City Research Online

City St George's, University of London

Citation: Seddiq, M., Alnajideen, M. & Navaratne, R. (2025). Thermal Transient Performance of PEM Fuel Cells in Aerospace Applications: A Numerical Study. Energy & Fuels, 39(16), pp. 7876-7889. doi: 10.1021/acs.energyfuels.4c04834

This is the published version of the paper.

This version of the publication may differ from the final published version. To cite this item please consult the publisher's version.

Permanent repository link: https://openaccess.city.ac.uk/id/eprint/36973/

Link to published version: https://doi.org/10.1021/acs.energyfuels.4c04834

Copyright and Reuse: Copyright and Moral Rights remain with the author(s) and/or copyright holders. Copies of full items can be used for personal research or study, educational, or not-for-profit purposes without prior permission or charge, unless otherwise indicated, provided that the authors, title and full bibliographic details are credited, a hyperlink and/or URL is given for the original metadata page and the content is not changed in any way. For full details of reuse please refer to City Research Online policy.

City Research Online: http://openaccess.city.ac.uk/ publications@citystgeorges.ac.uk

energy&fuels

Open Access

This article is licensed under CC-BY 4.0

pubs.acs.org/EF

Article

Thermal Transient Performance of PEM Fuel Cells in Aerospace Applications: A Numerical Study

Mehdi Seddiq, Mohammad Alnajideen,* and Rukshan Navaratne

Cite This: *Energy Fuels* 2025, 39, 7876−7889

Read Online

ACCESS | Metrics & More | Article Recommendations | Supporting Information

ABSTRACT: Polymer electrolyte membrane fuel cells (PEMFCs) are gaining attention as viable energy carriers for future aerospace propulsion systems due to their high-power density, lightweight and compact design, zero emissions, scalability, quiet operation, and relatively reliable performance. However, maintaining optimal performance and durability under transient thermal conditions remains a critical challenge, particularly in aerospace environments. Despite extensive research on PEMFCs, the transient thermal effects remain underexplored. This study employs a validated numerical simulation model to investigate the transient responses of a PEMFC subjected to thermal shock cycles, where the bipolar plate walls experience abrupt temperature drops to 10 °C for durations of 3 to 19 s. The simulation model was benchmarked against experimental data from the literature, demonstrating deviations of less than 10% in the polarization curves, confirming its reliability for predicting transient behaviors. Results reveal that during these thermal shocks, the current density decreases by approximately 15%, from 9263 A/m^2 at 50 °C to 7709 A/m^2 at 10 °C, with recovery times exceeding 4 s. Significant deviations were observed in oxygen concentration, particularly at the cathode catalyst layer, where minimum levels decreased by over 20%. Similarly, the water content in the membrane showed an overshoot above steady-state levels postrecovery, remaining elevated for extended periods. Liquid water saturation in the gas diffusion layers (GDLs) increased significantly near the hydrogen inlets during cold conditions, obstructing reactant flow and further impacting performance. This study provides detailed predictions of the steady-state and transient responses of PEMFCs to temperature reduction cycles. The findings contribute to advancing thermal management strategies and improving system resilience under transient conditions, thereby addressing a key challenge in sustainable aviation.

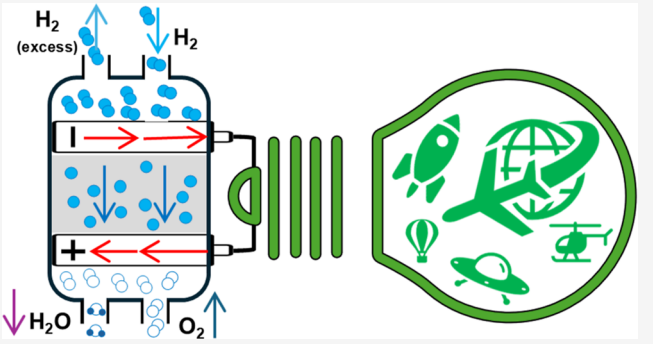

Downloaded via 138.40.32.22 on March 2, 2026 at 14:24:24 (UTC).
See https://pubs.acs.org/sharingguidelines for options on how to legitimately share published articles.

1. INTRODUCTION

Polymer electrolyte membrane fuel cells (PEMFCs) are increasingly considered a promising energy solution for aerospace applications due to their high-power density, lightweight design, and environmentally friendly operation.[1−5] Unlike conventional fuel technologies, PEMFCs produce only water as a byproduct,[6] aligning with global initiatives to reduce carbon emissions and enhance sustainability in aviation. Their compact size and scalability enable integration into a variety of aerospace platforms, ranging from unmanned aerial vehicles (UAVs) to commercial aircraft.[7] Moreover, PEMFCs operate quietly and efficiently under varying environmental conditions, making them suitable for both commercial and military applications where noise reduction and stealth are critical.[8−11]

Despite their advantages, widespread adoption of PEMFCs in aerospace remains challenging due to high production costs, primarily associated with platinum catalysts, and durability concerns linked to membrane and catalyst degradation.[12−16] This degradation can occur through chemical, mechanical, and thermal pathways, leading to a reduction in performance and lifespan. Effective water and thermal management are also essential to ensure optimal performance. Excess water accumulation can block reactant gases, whereas inadequate hydration can reduce membrane conductivity, impacting fuel cell efficiency.[17,18]

Unlike automotive PEMFCs, which are optimized for rapid start-up and frequent load variations,[19] aerospace PEMFCs must function reliably under extreme altitudes, variable temperatures, and reduced atmospheric pressure. This necessitates robust design strategies that prioritize durability and fuel efficiency over cost, given the premium placed on reliability and safety in aerospace missions.[20] The design must accommodate stringent weight and volume constraints while maintaining stable performance in low-pressure environments[11,21]. In contrast, automotive PEMFCs focus on optimizing volumetric and gravimetric power density to reduce

Received: October 4, 2024
Revised: March 14, 2025
Accepted: April 7, 2025
Published: April 15, 2025

© 2025 The Authors. Published by American Chemical Society

system weight and enhance vehicle range, as well as minimizing costs to ensure market competitiveness. Advances in catalyst development, such as platinum group metal-free (PGM-free) catalysts, and improvements in membrane durability under varying operating conditions, are crucial to achieving these goals[18,19,22].

Automotive PEMFCs typically operate within stable environments but must handle frequent load variations due to acceleration and deceleration cycles. Efficient waster and heat management is crucial to prevent membrane flooding or drying, particularly under subfreezing or high-humidity conditions.[23,24] Thermal management systems maintain optimal operating temperatures to ensure consistent performance. Aerospace PEMFCs, however, face unique environmental challenges, including reduced oxygen availability at high altitudes and extreme temperature variations.[25] Lower oxygen partial pressure necessitates advanced air compression systems or oxygen-enrichment systems to maintain adequate reaction kinetics.[26] Aerospace PEMFCs often incorporate specialized materials and coatings to withstand radiation or corrosive atmospheric conditions.[27,28]

Durability remains a concern for PEMFCs applications in automotive and aerospace sectors. Automotive PEMFCs have lifespans of approximately 5000 to 8000 h, matching typical vehicle life expectancy.[29−31] Their design focuses on mitigating degradation, membrane thinning, and gas diffusion layer wear often caused by dynamic load cycling and frequent start−stop conditions.[32,33] In contrast, aerospace PEMFCs require significantly longer operational lifespans with minimal maintenance, particularly for space missions or UAVs, where repairs are infeasible.[34] These systems are designed to endure continuous operation over tens of thousands of hours, necessitating superior material stability and innovative strategies to mitigate mechanical and chemical degradation.[35] Several studies have discussed differences and challenges between automotive and aerospace PEMFC designs.[24,28,34,36]

PEMFCs generally operate at relatively low temperatures, which limit their performance and efficiency in certain applications.[37] Increasing operating temperatures can enhance performance but presents material and engineering challenges, such as maintaining membrane hydration and stability.[37] In addition, hydrogen storage and distribution logistics further complicate large-scale PEMFC deployment,[38,39] and safety concerns due to hydrogen's flammability necessitate rigorous management.[39,40]

Advances in materials science and engineering are enabling more efficient and cost-effective PEMFCs. Innovations in catalysts,[41,42] membrane durability,[42,43] and system integration[42,44] are steadily reducing costs and improving the viability of this technology. A summary of the key challenges (or barriers) is presented in Figure S1 (appendix A), identifying essential research and development prioritize for improving PEMFC performance and ensuring material integrity before commercial deployment.

In a single PEMFC (Figure S2,[45] appendix A), electricity generation occurs via reaction between oxygen and hydrogen, separated by a porous membrane with a thin catalyst layer (CL). At the anode (fuel side), hydrogen splits into protons and electrons; protons migrate through the membrane to the cathode, reacting with oxygen to produce water. Electrons flow through conductive bipolar plates (BP), generating electrical current for external circuits. Channels within bipolar plates distribute hydrogen and oxygen, while the gas diffusion layer (GDL) between the plates and membrane ensures even gas distribution, manages excess water, and conducts electricity. Individual PEMFCs generate approximately 0.5−0.8 V each,[46] requiring stacking of multiple cells to increase voltage and power. The combined structure (membrane, catalyst layers, and GDL) forms the Membrane Electrolyte Assembly 11 11. Auxiliary systems, including water and thermal management systems, support PEMFC operation. Proper humidity control prevents membrane dehydration or water blockage in gas channels.[47] Thermal management systems regulate temperature, maintaining the optimal performance range.[48] Understanding fuel cell performance under steady-state and transient conditions requires experimental and computational investigations.

Zhang et al.[49] experimentally studies the dynamic behavior of high-temperature PEMFCs under load variations, identifying hysteresis in polarization curves, particularly evident at lower currents and higher voltages. Saleh et al.[50] experimentally validated a mathematical model for a self-humidifying PEMFCs, focusing on voltage and temperature changes under varying loads. While some researchers adopt semiempirical models for simplicity and parameter fitting,[51−53] such models typically offer limited insights into internal fuel cell processes. For instance, Akimoto and Okajima[54] employed a semiempirical approach to assess the impact of temperature on voltage−current density relationships.

Dynamic models address transient fuel cell behavior in response to changing loads or operating conditions,[55] often simplifying the computational complexity by using reduced-dimensional approaches. Pathapati et a.[56] proposed a dynamic model to study variations in cell voltage, temperature, pressure, and inlet flow rates in response to sudden load changes. Shamardina et al.[57] developed a dynamic model to evaluate electrochemical impedance under step changes in potential, current and current interruptions.

Rabbani and Rokni[58] studied transient nitrogen accumulation in PEMFC anodes using commercial software tools, exploring purging strategies to enhance performance. Lan and Strunz[59] used equivalent electric circuit modeling to study auxiliary systems during transient operations, whereas Zou and Kim[60] employed MATLAB- Simulink for fuzzy controller-based thermal management. Similarly, Ceylan and Devrim[61] developed a MATLAB-Simulink dynamic model incorporating fuel cell systems with solar energy integration, batteries, electrolyzers, and economic analysis.

Comprehensive understanding of electricity generation in PEMFCs requires detailed modeling of fluid dynamics and concentration distribution through full transport equations, despite high computational demands. Yan et al.[62] implemented a three-dimensional model to study transient current density and mass transport in serpentine-layout channel designs. Goshtasbi et al.[63] investigated transient responses to voltage and current variations, highlighting the critical role of water transport and microstructural features. Bodner et al.[64] examined hydrogen starvation effects during start-up via ANSYS-Fluent, proposing a scheme for larger time steps in computations. Wang et al.[65] presented a two-dimensional model to investigate the transient effects of current change on parameters such as temperature and humidity at cathode catalyst layer, membrane water content, and output voltage, exploring how different channel widths impact results. Kravos et al.[66] presented a two-phase transient model, addressing

https://doi.org/10.1021/acs.energyfuels.4c04834
Energy Fuels 2025, 39, 7876−7889

crucial transport phenomena within segmented membrane electrode assemblies.

Temperature significantly influences PEMFC performance, as effective heat management is essential for optimized operation. Elevated temperatures enhance reaction kinetics but may increase voltage losses.[67,68] Operating at higher temperatures reduces liquid water blockage through enhanced vaporization, leveraging generated heat.[69] Conversely, lower temperatures simplify water management and accelerate start-ups, while reducing corrosion and thermomechanical stress, extending lifespan.[70] Therefore, understanding temperature effects on membrane conductivity and water transport diffusivity is vital. Yan et al.[71] experimentally analyzed PEMFC cold start-up behavior at different temperatures, assessing irreversible performance degradation at subfreezing temperatures. Adzakpa et al.[72] developed a three-dimensional dynamic model addressing steady-state temperature nonuniformities and transient responses in air-cooled fuel cells. Ondrejička et al.[73] numerically investigated steady-state temperature impacts on voltage losses, identifying optimal operating conditions across different voltage ranges and transient power fluctuations.

Current research on PEMFCs has primarily focused on steady-state performance, leaving transient thermal behavior underexplored. Understanding how PEMFCs respond to sudden temperature changes is crucial for improving system resilience and reliability in aerospace applications. This study addresses this gap by investigating the transient thermal performance of PEMFCs under temperature drop cycles. Using a validated numerical model, we analyze the effects of abrupt temperature reductions on key performance parameters, including current density, reactant distribution, and water content. The insights gained from this study contribute to optimizing thermal management strategies and enhancing PEMFC durability in real-world aerospace scenarios.

2. METHODOLOGY

2.1. PEMFC: Simulation Setup. This study employs a PEMFC consisting of a parallel layout with a counter-flow configuration (Figure S3, Appendix). The choice of this design is guided by its advantages under steady-state, moderate-load conditions. Parallel channel designs provide lower pressure drops than serpentine or interdigitated flow fields, thus reducing auxiliary power losses and enhancing system efficiency, which is vital for energy-limited aerospace applications.[74−77] Counterflow arrangements further improve thermal and reactant distribution, reducing temperature gradients and mitigating potential hotspots or uneven water distribution, thus stabilizing performance under moderate current densities.[78−82] The result is a more stable cell performance under low to moderate current densities, as observed in previous studies.[78,81,83−85] Although parallel-counterflow configurations might not outperform serpentine channels at high loads or transient conditions, their strengths align closely with aerospace application priorities: lightweight systems, minimal energy losses, and operational stability.[86−89] As noted in previous work,[78,79,81,83−85,90−92] the parallel-counterflow combination offers a promising trade-off between efficiency, simplicity, and reliability, which are essential for aerospace systems constrained by weight and operational stability.

Table 1 provides cell specifications, and Table 2 illustrates simulation conditions for the flows at the cell channels' inlets.

Table 1. Specifications of the PEMFC Used in This Study

parameter	value	unit
cell planar dimensions	30.00 × 30.00	mm × mm
channel height	1.00	mm
channel width	1.00	mm
bipolar plate (BP) maximum thickness	1.50	mm
GDL thickness	300.00	μm
CL thickness	12.90	μm
membrane thickness	108.00	μm
GDL porosity	0.60	
CL porosity	0.20	
CL absolute permeability	2.00×10^{-13}	m^2
GDL absolute permeability	3.00×10^{-12}	m^2
anode reference current	10000.00	A/m^2
cathode reference current	10.00	A/m^2
anode/cathode activation energy	8314.34	J/mol
temperature for reference current	70.00	°C
steady-state voltage	1.23	V
BP material	Carbon graphite	

Table 2. Flow Conditions at the Channel Inlets for all Simulations in This Study

parameter	value	unit
pressure (both sides)	1.00	bar
inlet temperature (both sides)	50.00	°C
inlet relative humidity for anode side	100.00	%
inlet relative humidity for cathode side	50.00	%

Uniform mass fluxes with specified mole fractions have been considered at the inlets. ANSYS 2021-R1 software was employed to simulate the chemical reaction and calculate species concentration variations, fluid velocity, pressure, temperature changes and electricity generation within a single cell. The meshing and numerical solution procedure for cell simulations is available in the Appendix.

The chosen cell planar dimensions (30.00 × 30.00 mm) represent a simplified geometry suitable for numerical modeling and detailed computational analyses. While this smaller scale may limit the direct representation of thermal gradients found in practical, full-scale PEMFC stacks used in aerospace applications, it remains effective for investigating the fundamental transient thermal responses and associated performance dynamics. A comprehensive evaluation of larger-scale cells or stack-level modeling would be beneficial for further validation and for capturing the effects of realistic temperature distributions in actual operational environments.

2.2. PEMFC: Computational Configuration. Inlet mass flow rates include vapor and dry reactant mass flow, calculated using stoichiometric ratios (anode: 1.6, cathode: 2.5 at a reference current density of 10,000 A/m^2). Actual stoichiometric ratios increase as output current densities decrease. Constant temperature boundary conditions (50 and 10 °C) are applied to the bipolar plate (BP) walls, including the back terminal surfaces, side walls perpendicular to the membrane, and walls around the channels. These walls are assumed to be controlled by the thermal management system. Conjugate conditions are applied at the BP-GDL interface. A pressure outlet boundary condition is used for the outlets. Except for BP walls, all other side boundaries surrounding the membrane electrode assembly 11 are considered walls with zero fluxes for pressure, temperature, species, and electric potential. The cell

https://doi.org/10.1021/acs.energyfuels.4c04834
Energy Fuels 2025, 39, 7876−7889

terminal voltage is kept constant at 0.55 V, a typical operating voltage for fuel cells close to the maximum power point. High current densities at this voltage result in liquid water formation in parts of the GDL and CLs. Current density, an output quantity, is calculated by integrating over the back surface of the bipolar plates, and average values from the anode and cathode are reported.

To study transient and steady-state effects of temperature changes, a series of numerical experiments with different temperature cycles are conducted. Normally, the BP wall temperature is the same as the inlet flow temperature (50 °C). A thermal shock is applied by reducing the BP external walls temperature to 10 °C, creating spatial temperature gradients within the stack during transient conditions. The temperature then returns to the original value, completing a thermal cycle. The temperature is represented by $T_{CL,c}$ and $T_{CL,a}$, referring to the average of maximum and minimum temperatures within the cathode and anode catalyst layers, respectively. In this study, the bipolar plates are modeled with constant temperature conditions of 50 and 10 °C to reflect their high thermal conductivity of graphite, which minimizes temperature differences across the plates. These specific temperatures represent typical operating and extreme cold-start conditions relevant to aerospace applications. This simplification enables the study to isolate and analyze the transient thermal effects at the interface between the bipolar plates and other components without introducing additional complexity from internal temperature gradients within the plates.

2.3. PEMFC Model. Fluent software, along with the PEMFC module, is used to compute the two-phase multispecies fluid flow, heat transfer, and charge transport in a three-dimensional domain. The flow is considered laminar (Reynolds number is approximately 418) and incompressible, and the equations for liquid water transport are included for both porous parts and channels. The basic equations[93,94] used for the conservation of mass and momentum are as follows

$$\frac{\partial \varepsilon\rho}{\partial t} + \nabla\cdot(\varepsilon\rho \boldsymbol{u}) = S_{m,i} \tag{1}$$

$$\left(\frac{\partial}{\partial t}(\varepsilon\rho \boldsymbol{u}) + \nabla\cdot(\varepsilon\rho \boldsymbol{u}\boldsymbol{u})\right) = -\nabla p + \nabla\cdot(\overline{\overline{\tau}}) + \boldsymbol{F} \tag{2}$$

whereas ρ, $\boldsymbol{u}$, ε, $\overline{\overline{\tau}}$ and $\boldsymbol{F}$ represent the density, velocity vector, porosity, stress tensor, and external body forces, respectively. $S_{m,i}$ denotes the rate of mass density change for the species i due to its consumption or production. This value is negative for hydrogen and oxygen in anode and cathode catalysts, positive for water in cathode catalyst, and zero otherwise.

Equations 1 and 2 are not solved for the bipolar plates (BPs), which are solid structures, nor for the membrane. In the membrane and catalyst layers (CLs), water exists in the form of a dissolved phase, and its transport in these regions is calculated using alternative equations based on water content. The distribution of species is calculated by solving separate transport equations for each species i, as given by Equation (3)

$$\frac{\partial}{\partial t}(\varepsilon\rho Y_i) + \nabla\cdot(\varepsilon\rho \boldsymbol{u} Y_i) = -\nabla\cdot(\boldsymbol{J}_i) + S_{Y_i} \tag{3}$$

where Y_i is the local mass fraction for the species i, $\boldsymbol{J}_i$ is a vector denoting the diffusive mass flux for the species i, and S_{Yi} is the source term. The diffusion term $\mathbf{J}_i$ is governed by gradients of concentration and temperature.

The Full Multicomponent Diffusion method, which accounts for the species binary mass diffusion coefficients and thermal diffusion coefficients, has been used to enhance the accuracy of the diffusion flux calculation. The source term S_{Yi} includes the production/consumption terms caused by chemical reaction and a term for addition from the dispersed phase. The species transport equation is solved for all species except for nitrogen, which is calculated by a simpler equation (eq 4). The nitrogen concentration is typically determined using an assumption of its inert behavior, simplifying the model.

$$Y_{N_2} = 1 - \sum_{i=1}^{n-1} Y_i \tag{4}$$

where $n = 4$, is the number of species.

The transport equations for liquid water in the gas diffusion layers (GDL) and catalyst layers (CLs), and membrane are described based on liquid saturation, s which is defined as the fraction of the pore space filled by the liquid water. The liquid saturation s is calculated using a transport equation as follows

$$\frac{\partial}{\partial t}(\varepsilon\rho_l s) = \nabla\cdot\left(\frac{\rho_l K}{\mu_l}\nabla p_l\right) + S_{gl} - S_{ld} \tag{5}$$

where; ρ_l and μ_l are the density and dynamic viscosity of the liquid water, respectively. K is the effective permeability which is the production of the absolute and relative permeabilities, S_{gl} is the rate of mass exchange between gas and liquid phases, and S_{ld} is the rate of mass exchange between liquid and dissolved phases.

The calculation of liquid water transport in gas channels provides more accurate results by predicting the pressure drop increase due to the presence of liquid water

$$\frac{\partial}{\partial t}(\rho_l s) + \nabla\cdot(\rho_l \boldsymbol{u}_l \nabla s) = \nabla\cdot(D_l \nabla s) \tag{6}$$

where $\mathbf{u}_l$ is the velocity of the liquid water in channels, and it is a fraction of the local velocity of the gas. D_l is the liquid water diffusion coefficient in the channels.

The energy equation for the single-phase regime is given by

$$\frac{\partial}{\partial t}(\rho e) + \nabla\cdot(\rho \boldsymbol{u} h) = \nabla\cdot(k\nabla T) + S_E \tag{7}$$

where e and h are the internal energy and enthalpy, T is the temperature, k is the thermal conductivity and S_E is the thermal source term which includes heat generation caused by the chemical reaction and ohmic losses.

The electric potential is calculated based on transport equations for the solid and membrane phases separately

$$\nabla.\ (\sigma\nabla\Phi) + R = 0 \tag{8}$$

where Φ is the electric potential, σ is the electric conductivity, and R is the volumetric transfer current. R is zero all over the domain except for the CLs. It depends on the molar concentrations of the reactants and temperature and is calculated based on a general formulation of the Butler–Volmer function

$$R_a = \zeta_a j_a \left(\frac{C_{H_2}}{C_{H_2,ref}}\right)^{0.5} \left(e^{a_a^a F\eta_a/RT} - e^{a_c^a F\eta_a/RT}\right) \tag{9}$$

https://doi.org/10.1021/acs.energyfuels.4c04834
Energy Fuels 2025, 39, 7876−7889

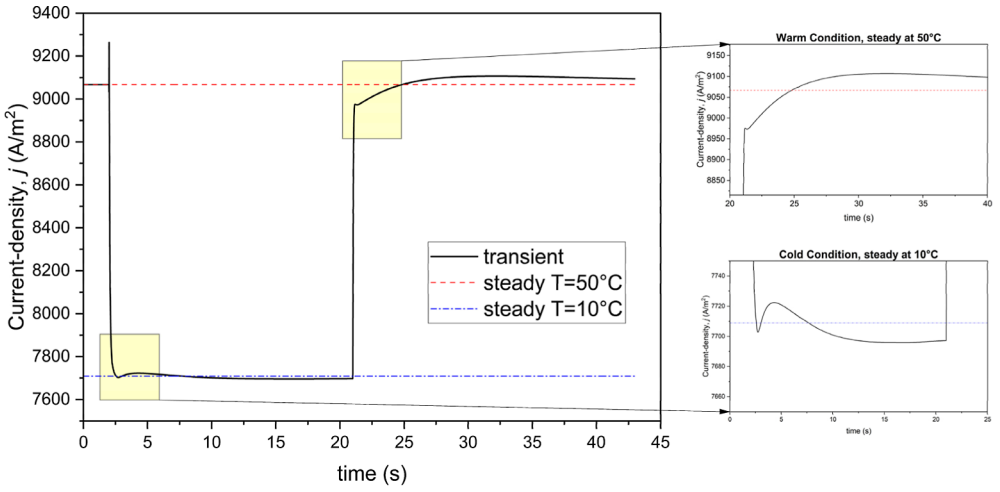

Figure 1. Variations in current density during the transient simulation with a single thermal cycle (inset figures show detailed views for specific time intervals at cold and warm steady-state conditions).

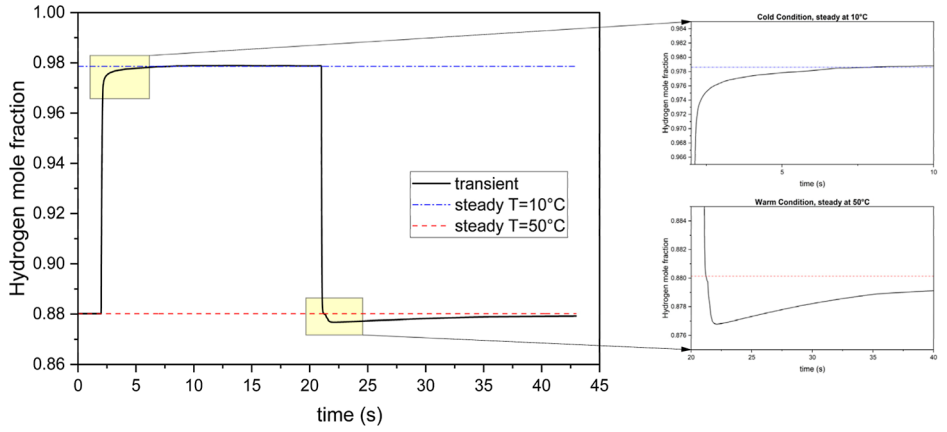

Figure 2. Minimum mole fraction of hydrogen at anode catalyst layer-gas diffusion layer during the transient simulation with a longer-period thermal cycle (inset figures show detailed views for specific time intervals at cold and warm steady-state conditions).

$$R_c = \zeta j_c \left(\frac{C_{O_2}}{C_{O_2,ref}} \right) \left(-e^{a_a^c F \eta_c / RT} + e^{a_c^c F \eta_c / RT} \right) \tag{10}$$

where indexes a and c denote anode and cathode sides respectively, ζ is specific active surface area, j is the reference exchange current density explained below, C is the local concentration for a reactant (oxygen in cathode and hydrogen in anode), index ref denotes the reference concentration, a^a and a^c are the transfer coefficients of anode and cathode respectively (each anode and cathode has its set of transfer coefficients), $F = 96485$ C/mol is the Faraday constant and η is the surface overpotential. The reference exchange current density is a function of the temperature

$$j_a = j_a^{ref} e^{-E_a/RT(1-T/T_a^{ref})} \tag{11}$$

$$j_c = j_c^{ref} e^{-E_c/RT(1-T/T_c^{ref})} \tag{12}$$

where j^{ref} is the value at the reference temperature T^{ref}, and E is the electric potential.

Further details about the governing equations can be found in ANSYS-Fluent 2021 R1 Theory Guide.[95]

3. RESULTS AND DISCUSSIONS

3.1. Validation of the Simulation Model. To validate the simulation model developed for this study, a mesh independence study was conducted to select an appropriate mesh size with a reasonable number of computational elements. For model validation, the experimental study of Najmi et al.[96] with a parallel channel were used as benchmarks. The resulting voltage−current density relationships, known as the polarization curves, are shown and compared against the experimental data from the benchmark in Figure S4 (appendix). Compared to Najmi et al.,[96] the model shows agreement with a deviation of less than 10% in the range of 0.35−0.85 V. These deviations are considered acceptable, indicating that the results of the present model are in particularly good agreement with the benchmark analysis. While the current model validation relies on steady-state experimental data due to limited availability of transient benchmarks, future studies will incorporate transient experimental validation to further confirm the accuracy of the transient predictions.

3.2. Single Thermal Shock. In the first simulation, while the fuel cell operation is in a fully steady state, at $t = 2s$, the BP walls are dropped to 10 °C, and they remain at this temperature for 19 s. The temperature then returns to normal.

https://doi.org/10.1021/acs.energyfuels.4c04834
Energy Fuels 2025, 39, 7876−7889

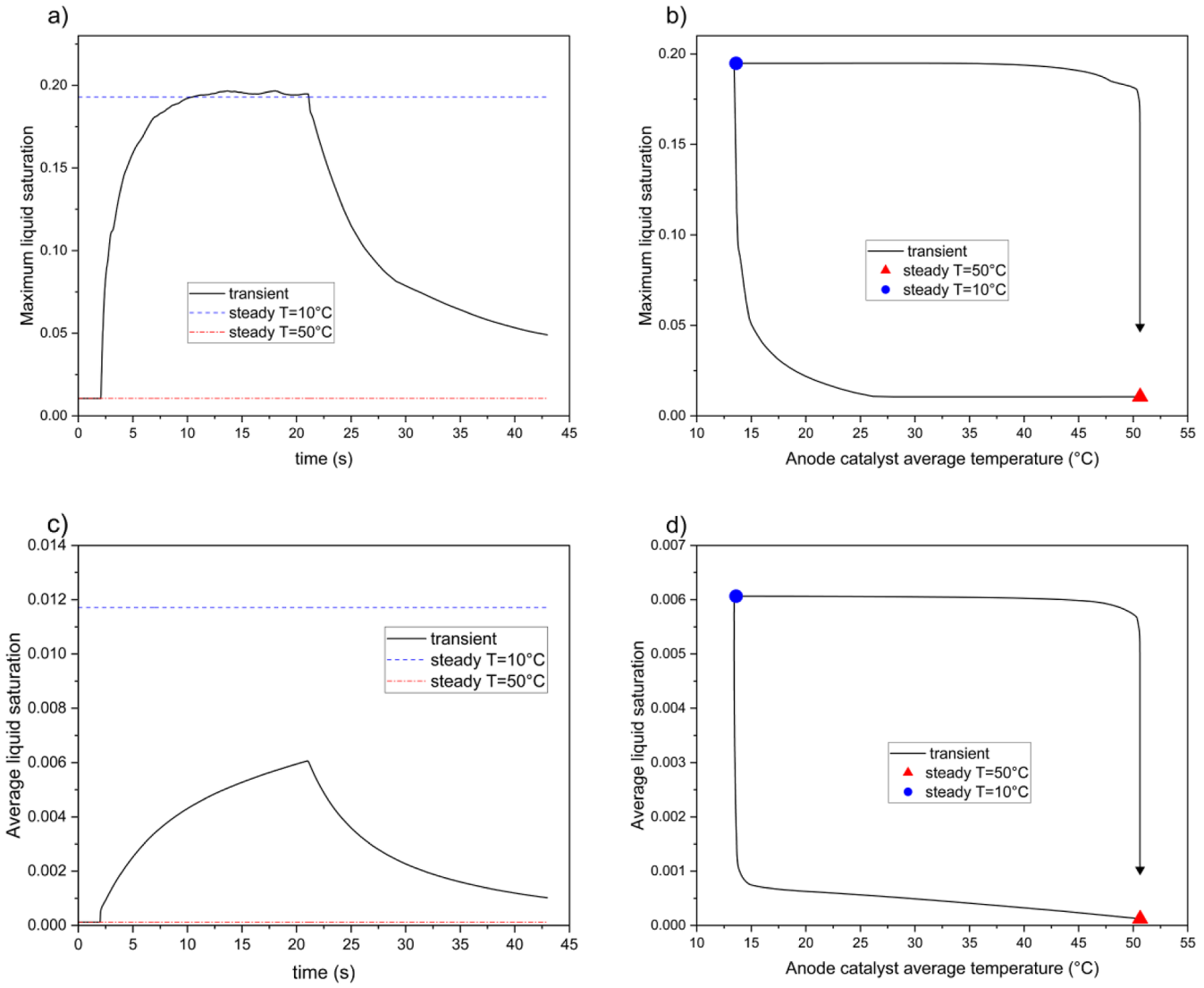

Figure 3. Variations of liquid water saturation inside the anode GDL during a long-period thermal cycle; (a,b) are the maximum liquid saturation over time and with temperature changes, respectively; (c,d) are the average liquid saturation over time and with temperature changes, respectively.

Another simulation is also conducted with a shorter period of 3s for the cold temperature to study the effect of the cycle duration. The variations in the average maximum and minimum temperatures within the cathode catalyst layer, $T_{CL,c}$ are shown in Figure S5 (appendix). After the temperature drops at the BPs walls, CL is affected by more than 6 °C reduction within 10 ms. In about 1*s*, the average temperature is reduced by approximately 37.5 °C and to the end of the cold conditions at t = 21 s, it undergoes a further reduction of only 0.2 °C.

Figure 1 illustrates the current density, j, of the simulated fuel cell. Under steady-state conditions at 10 °C, the current density is 7709 A/m^2, which is significantly lower than the 9263 A/m^2 observed at 50 °C. This reduction indicates that the fuel cell delivers ∼15% less power during the colder part of the cycle. During cold conditions, the current density stabilizes slightly above the steady-state value. Afterward, the fuel cell underperforms for 3.8 s, with the current density 1% below the normal steady-state value. A shorter cold cycle (see Figure S6) reduces the intensity of underperformance but extends its duration to 4.8 s. By t = 31 s, the current density remains 0.3% above the steady-state value.

As the simulation began, the fuel cell operated steadily until the temperature of the BP walls was abruptly reduced to 10 °C. This sudden drop in temperature triggered a series of changes within the cell. Notably, the minimum hydrogen mole fraction f_{H_2}, at the anode catalyst layer-gas diffusion layer (CL-GDL) interface increased significantly. This increase remained stable until the temperature returned to normal. However, the return to normal conditions initiated a rapid reduction in f_{H_2}, pushing it below the steady-state levels. Gradually, over time, f_{H_2} began to approach its steady-state value once again. This dynamic behavior had a profound impact on the current density within the cell. As can be seen in Figure 2, the minimum hydrogen mole fraction at the anode CL-GDL interface clearly demonstrates these fluctuations. The data suggests that the initial low current density following the thermal shock correlates with the observed decline in f_{H_2} values below the steady-state levels. This correlation highlights the sensitivity of the fuel cell's performance to changes in the hydrogen mole fraction at critical interfaces.

During cold conditions, the increase in the minimum hydrogen mole fraction is primarily due to the lower current

https://doi.org/10.1021/acs.energyfuels.4c04834
Energy Fuels 2025, 39, 7876−7889

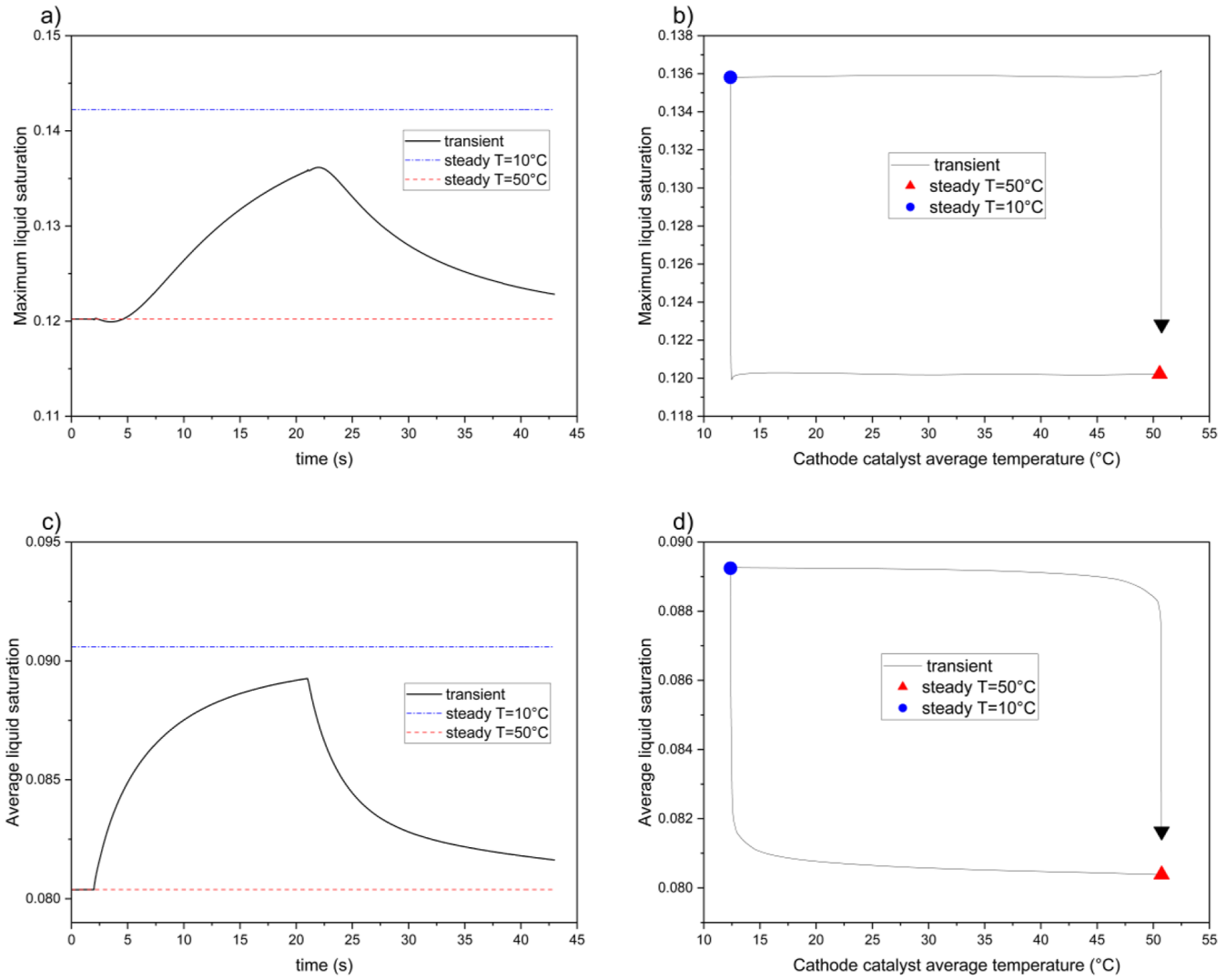

Figure 4. Variations of liquid water saturation inside the cathode GDL during a long-period thermal cycle; (a,b) are the maximum liquid saturation over time and with temperature changes, respectively; (c,d) are the average liquid saturation over time and with temperature changes, respectively.

generation and reduced hydrogen consumption rates. In addition, since the anode inlet is fully humidified, the lower temperatures cause more water to saturate, leaving less water vapor in the pores. This results in a higher mole fraction of hydrogen. To understand the causes of the reduction in hydrogen mole fraction after the cold temperature period, we can look at Figure S7 (appendix), which shows the liquid water saturation (s) contours in the anode's CL-GDL at t = 21 s. This moment is shortly before the temperature returns to normal, and the fuel cell's performance is steady at 10 °C. Before the temperature drops, the maximum water saturation in the anode occurs near the edge, close to the inlet, with no significant variations in saturation elsewhere. However, when the BP' walls and channel walls are cold, and the inlet flow is fully wet at 50 °C, water condenses along the channel, leading to considerable saturation around the inlet. This increase in condensed water within the anode's porous media, especially near the inlet, remains long after the temperature normalizes. Liquid water obstructs parts of the hydrogen passage near the inlet, where fresh hydrogen is supplied. As a result, hydrogen concentrations decrease downstream, contributing to the observed reduction in hydrogen mole fraction.

Figure 3 shows the maximum and average values of liquid water saturation (s) inside the anode GDL during the simulation. The thermal cycle causes a significant increase in the amount of saturated water within the anode. The maximum saturation is notably higher than the average saturation and exhibits a quicker rise toward the steady-state level (see Figure 3a,c). By the end of the cold conditions, the maximum saturation reaches the steady-state value, despite the average saturation lagging behind. Both curves respond immediately to the thermal shock and start to decline once the temperature returns to normal. However, while the maximum saturation grows rapidly in response to the temperature reduction, the reduction rates of both maximum and average saturations are slow when the temperature normalizes. The anode average temperature curves indicate a hysteresis between saturation values as the temperature varies. Although the saturation threshold is linked to temperature, the saturation changes only slightly during temperature fluctuations. This phenomenon can be explained by two key factors. First, the latent heat of condensation and evaporation for water is high, meaning that even a small change in the amount of saturated water requires considerable heat absorption or rejection. Consequently, condensation and evaporation occur

https://doi.org/10.1021/acs.energyfuels.4c04834
Energy Fuels 2025, 39, 7876−7889

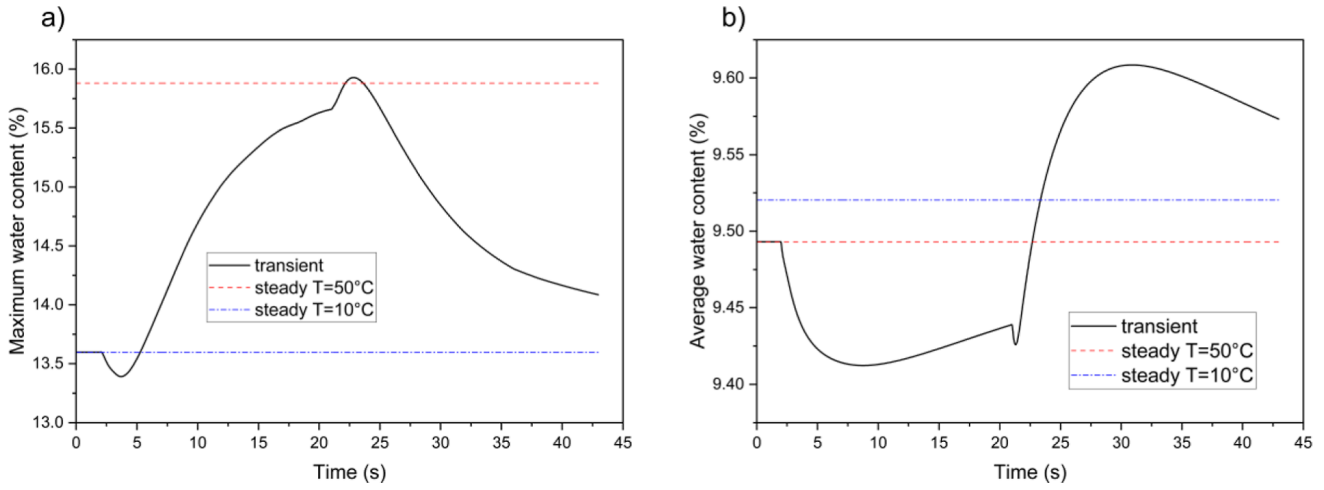

Figure 5. Local water content in the membrane for the case with a long-period thermal cycle; (a) maximum values, (b) average values.

on a time scale longer than temperature changes. Second, in this simulation, the current density follows the temperature variations. As the temperature decreases, less current is generated, resulting in lower water production.

The water saturation distributions in the cathode also provide valuable insights. Figure S8 (appendix) shows the contours for two instances: (a) before the temperature reduction, where conditions are steady at 50 °C, and (b) near the end of the low-temperature period, where conditions are close to steady state at 10 °C. At the normal temperature of 50 °C, saturation is lowest near the inlet because the inlet flow has only 50% relative humidity, and water produced by the reaction is added to the flow as it moves downstream. Liquid water tends to form mainly adjacent to the edges where only one branch of the channel is nearby to carry the excess water. There is also a considerable amount of liquid water close to the outlets where the water generated upstream accumulates. When the temperature is reduced, the relative humidity at the inlet increases, leading to regions with higher water saturation close to the inlet. The areas with low saturation values shift from the inlet toward the downstream sections of the interior branches, close to the downstream collector channel (the vertical channel on the left, as shown in Figure S3 in the Appendix).

Figure 4 presents the temporal curves for liquid water saturation inside the cathode GDL. The patterns and amounts of saturation differ between the cathode and anode sides due to water production in the cathode catalyst layer (CL) and less humidity being introduced at the inlets. At the beginning of the cold conditions, the curve for maximum saturation in the cathode decreases but soon starts to increase. Interestingly, it continues to rise for about 1 s after the cold conditions end, although it remains substantially lower than the steady-state value. This behavior is similar to what is observed in Figure 3a for the maximum water content in the membrane, suggesting a strong association between the maximum water content in the membrane and the maximum liquid water on the cathode side. The curve for average saturation, on the other hand, shows a faster response to temperature changes. As the temperature drops, the average saturation increases rapidly. Immediately after conditions return to normal, the average saturation begins to decline.

Figure S9 illustrates the temporal variations of the minimum oxygen mole fraction, f_{O_2} at the cathode CL-GDL interface. Unlike the minimum hydrogen mole fraction, which shows a different pattern during cold conditions, the minimum f_{O_2} is considerably reduced. This is in stark contrast to the behavior seen in Figure 2 for the minimum hydrogen mole fraction. In fact, the maximum and average f_{H_2} in the anode and the maximum and average f_{O2} in the cathode (see Figure S10 in the appendix) follow similar patterns to that of the minimum hydrogen. Figure S9 (appendix) also indicates that the minimum f_{O_2} at the cathode CL during the cold part of the transient cycle is significantly lower than its steady-state value under cold conditions. This suggests that the phenomenon is even more pronounced if the temperature is rapidly reduced. During most of the cold conditions, the minimum f_{O_2} exhibits an increasing trend, partially compensating for the dramatic initial drop after the temperature reduction. However, the rate of increase is low, and by the end of the cold conditions, the curve does not reach the steady-state value. This pattern is like the case with a shorter period of temperature reduction.

It is noteworthy that oxygen concentrations and current density are mutually interconnected. According to the reaction kinetics in eq 10, the rate of the chemical reaction in the cathode is proportional to the oxygen concentration, meaning higher f_{O_2} results in increased current density. However, an increase in current density leads to more oxygen consumption, which tends to reduce f_{O_2}.

The distributions of oxygen and nitrogen concentrations at a time close to the end of the cold conditions are presented in Figure S11 (appendix). Oxygen concentrations are lower in two regions: first, adjacent to the edges where only one branch of the channel supplies oxygen, and second, in a central-left area near the downstream collector channel (the vertical channel on the left, as shown in Figure S3), where the oxygen supply flow is weaker. Contours at t = 1.5 s during the steady-state condition at 50 °C (see Figure S12) indicate that while temperature variations change the mole fraction amounts, the locations of high and low concentrations remain almost unchanged. The oxygen mole fraction values near the edges are lower at both cold and normal temperatures but undergo further reductions during the cold cycle.

Several factors can potentially cause reductions in oxygen concentration. Comparing the oxygen and nitrogen concentrations in Figure S11 with the water saturation contours t =

https://doi.org/10.1021/acs.energyfuels.4c04834
Energy Fuels 2025, 39, 7876−7889

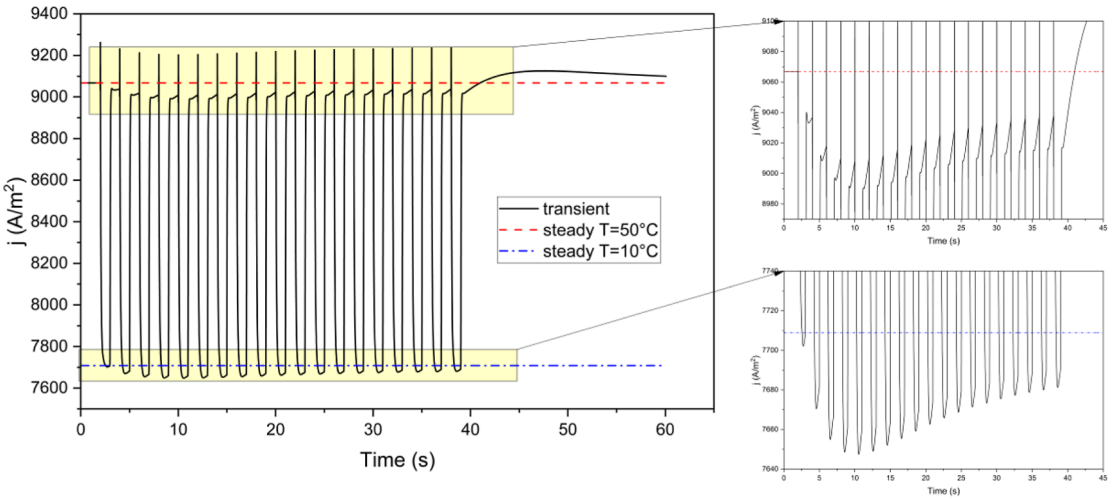

Figure 6. Current density during the case with repeated thermal cycles. Inset figures shows the specific ranges during the cycles.

20.5 s in Figure S8 provides valuable insights. The oxygen mole fraction is inversely correlated with the nitrogen mole fraction, indicating no significant blockage inhibiting gas flow, including oxygen. In addition, there is no substantial water production in the low-oxygen areas, suggesting no excess oxygen consumption in these regions. Overall, the low-oxygen regions are formed where the oxygen supply does not match its consumption.

The water content of the membrane is a crucial parameter that significantly influences the performance and efficiency of the fuel cell. Figure 5 illustrates the variations in both the maximum and average local values of water content within the membrane during the simulation. As shown in Figure 5a, the steady-state value of maximum water content at cold temperatures is notably higher than at normal temperatures. Initially, the maximum water content deviates from the steady-state value in response to temperature changes, followed by a rapid adjustment back toward the steady state, although the rate of change gradually decreases. This slower rate of change leads to a prolonged process of reaching the steady-state level. During the cold conditions, the maximum water content first declines but then begins to increase, although it does not reach the steady-state value by the end of the cold period due to the reduced rate of increase. Once the temperature returns to normal, the maximum water content undergoes rapid fluctuations before slowly approaching the steady-state value. The maximum water content is concentrated in a high-water content layer within the membrane, typically closer to the cathode side. At lower temperatures, this high-water content layer becomes thinner, while the gradients of water content from the surface to the core increase. This behavior may be attributed to the fact that in colder conditions, both the rate of mass exchange between liquid water and vapor and the diffusion coefficient of water content are reduced. Further research may be needed to clarify these observations.

The response of the average water content to rapid temperature changes, as shown in Figure 5b, highlights how sudden shifts in temperature can lead to significant departures from equilibrium conditions. Similar to the maximum water content, the average water content reacts in the opposite direction from the new steady-state values after a temperature change. When the temperature drops, the average water content quickly declines, moving away from the new steady-state value. Once the temperature returns to normal, the average water content rapidly increases, overshooting the steady-state value before slowly declining. Even as it decreases, the curve remains above the steady-state value for the remainder of the simulation.

Simulations with a shorter thermal cycle show that both the maximum and average water content in the membrane deviate from their normal values, and with a slow return to their steady-state levels, they remain significantly higher than normal throughout the entire simulation. The slight increase in current density after $t > 25$ s aligns with observations in Figures S11 and 5, where the minimum oxygen concentration and membrane water content (both maximum and average) surpass the steady-state values. To better understand which of these parameters is most influential, an additional simulation was conducted with the same conditions, except that the oxygen stoichiometric ratio was set to $\lambda_{O_2} = 1.5$. The results for i and the minimum f_{O_2} (Figure S13) demonstrate that despite the minimum falling below the steady-state value after the shock, the current density remained higher than the steady-state value. This indicates that the elevated membrane water content is likely the main factor responsible for the fuel cell's overperformance following the temperature cycle.

These results suggest that the minimum f_{H_2} at the anode CL, the minimum f_{O_2} at the cathode CL, and the average water content in the membrane are key parameters in the fuel cell's dynamics. They provide critical information useful for predicting performance. Furthermore, liquid water saturation in the GDLs offers valuable insights into the behavior of the system.

3.3. Repeated Thermal Shocks. In this study, 19 thermal shocks are introduced as shown in Figure S14 (Appendix), each lasting for 1 s with a 1 s interval between them. During each cycle, the temperature of the bipolar plate (BP) walls is reduced to 10 °C. The total duration of the cold conditions in this simulation is equivalent to that of the cold conditions in Section 3.2, allowing for meaningful comparisons between the single-cycle and multicycle cases. This comparison will help to better understand how the duration and frequency of the cycles impact performance and key parameters.

Figure 6 illustrates the variations in current density over time. Under multiple short thermal cycles, the fuel cell

https://doi.org/10.1021/acs.energyfuels.4c04834
Energy Fuels 2025, 39, 7876−7889

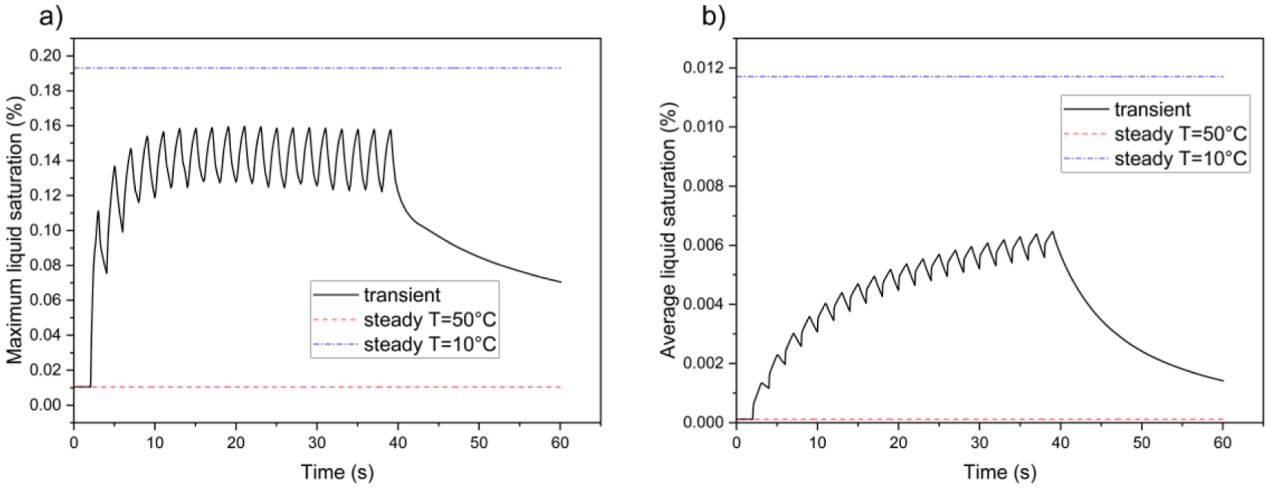

Figure 7. Variations of liquid water saturation (s) inside anode GDL in the case with repeated thermal cycles; (a) maximum water saturation vs time, (b) average water saturation values vs time.

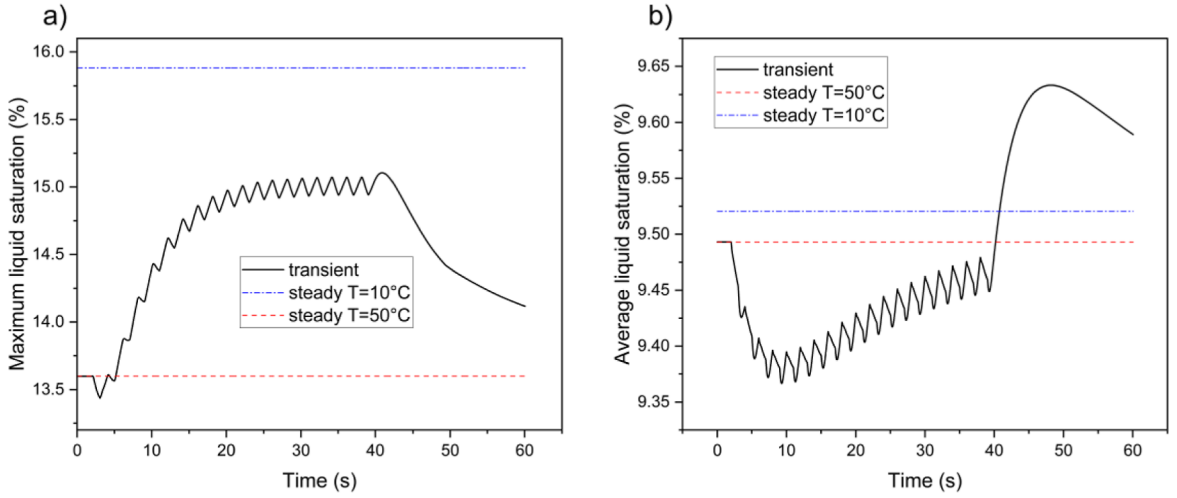

Figure 8. Local water content in the membrane for the case with repeated thermal cycles; (a) maximum values, (b) average values.

performance is worse than in the single-cycle case, with the current density falling substantially below steady-state levels for nearly the entire duration of the cycles. During thermal cycling, the average current density, j, in the low-temperature conditions decreases cyclically, meaning its value at a given point in one cycle is smaller than at the same point in the previous cycle. This decline continues until cycle 5, after which the current density begins to increase. A similar pattern is observed during normal temperature conditions, where the current density decreases until cycle 5 and then starts to rise. In cycle 5, both at low and normal temperatures, the current density is approximately 0.7% lower than the steady-state value at the corresponding temperature. After the final cycle, the current density surpasses the steady-state value and remains above it for the remainder of the simulation.

Figure 7 present the water saturation (s) curves in the anode GDL. After an initial rapid increase, the maximum water saturation reaches a cyclic stability that remains significantly lower than the steady-state value. The curve for the average water saturation shows a continuous cyclic rise, with temperature-dependent oscillations occurring within each cycle. However, the peak of this curve remains noticeably lower than the steady-state value under cold conditions.

The saturation curves for the cathode side are presented in Figure S15 (Appendix). Overall, both the maximum and average saturations exhibit temperature-dependent fluctuations within each cycle. However, saturation levels tend to increase toward the end of each cycle, and this upward trend persists throughout the remaining cycles. Regarding the maximum saturation, the first cycle follows a different pattern than the subsequent cycles. Similar to the previous case with a single long cycle, the maximum saturation initially decreases during the cold conditions of the first cycle, followed by a rise. A comparison between the $s-T$ curves of the first and last cycles reveals that the average saturation approaches cyclic stability by the last cycle. Most of the growth in maximum saturation occurs at the end of the cycles, coinciding with the return of the temperature to normal levels. Both curves begin to decline after the last cycle; however, the maximum saturation curve shows a slight delay before starting its descent.

When comparing the saturation curves between the single-cycle and multiple-cycle cases, and disregarding the fluctuations, the variation patterns for both maximum and average values show significant similarities. However, in the multiple-cycle case, the peaks of the curves are generally smaller. On the anode side, the curve for maximum saturation reaches a

https://doi.org/10.1021/acs.energyfuels.4c04834
Energy Fuels 2025, 39, 7876−7889

stability close to the steady-state point. In the multiple-cycle scenario, the additional liquid water formed during cold conditions remains in the porous media for a relatively long period. Moreover, changes in the amount of liquid water occur primarily when the temperature field is stabilized, a trend that is more pronounced in the case of long-period temperature cycles.

The dynamics of minimum oxygen mole fraction f_{O_2}, in relation to temperature throughout the simulation is illustrated in Figure S16 (appendix). As the temperature returns to normal, the curves for minimum, f_{O_2} fall below their respective paths during the temperature decrease phase. Interestingly, the curves for all cycles follow the same trajectory, including the case with a single 3 s cold cycle (Figure S16). The curve for the single cycle with 19 s of cold conditions is also displayed in the figure. Since the system has more time to approach steady-state conditions at the lower temperature during the longer single cycle, the minimum f_{O_2} curve shifts slightly upward, nearing equilibrium at 10 °C. Consequently, the minimum f_{O_2} depends almost entirely on the temperature and the direction of temperature change.

Figure 8 presents the curves for the maximum and average values of the local water content in the membrane. For the maximum value curve, aside from the first cycle, there is a cyclic increase where the maximum water content becomes progressively higher from one cycle to the next at similar points. Over time, the curve approaches cyclic stability, meaning that after a few cycles, the changes between cycles stabilize. The values at the end of each cycle become nearly identical to those of the previous cycle, indicating that the system has achieved steady oscillatory behavior.

The overall pattern of changes for both maximum and average values of the membrane water content is similar to that seen in the single-cycle case. However, with multiple cycles, the peak of the maximum water content is significantly lower than in the single long cycle, while the average values fluctuate within a wider range. This suggests that a long-period cycle tends to increase the gradients of water content within the membrane more than multiple short cycles. Even after cyclical stabilization, the maximum water content remains noticeably lower than the steady-state value under cold conditions.

The average water content during the cycles is also consistently lower than the steady-state value. However, after the initial rapid declines during the first few cycles, the average values begin to increase toward the steady-state level. Once the temperature cycles are completed, the average water content rises rapidly and stays above the steady-state level for the remainder of the simulation. The rate of return to equilibrium is significantly faster than in the single-cycle case. Cyclic variations in current density follow a similar pattern to the curve for the average membrane water content, suggesting that membrane water content plays a key role in influencing the fuel cell's performance throughout the cycles. It is important to note that our findings are consistent with those reported in several studies referenced in the literature of this research.

4. CONCLUSIONS AND FUTURE WORK

This study investigated the transient performance of a polymer electrolyte membrane fuel cell (PEMFC) in response to temperature variations, simulating conditions relevant to aerospace conditions. By applying thermal shocks to the bipolar plates' walls, the study revealed key insights into the dynamic response of the fuel cells. While the terminal voltage remained fixed, the current density was calculated as the primary output. The main findings are as follows:

- Temperature reductions significantly decreased current density and reactant consumption, particularly near the stack edges and downstream sections, where oxygen concentrations were lowest. Cold conditions also led to excess liquid water accumulation near hydrogen inlets, obstructing reactant flow.
- The membrane's water content exhibited transient deviations, with reduced water content during cooling and overshooting steady-state levels upon recovery. These variations, influenced by slow liquid water dynamics in porous media, emphasize the importance of managing water balance during normal cycles.
- Recovery patterns varied across cell parameters. After an initial decline in performance, the cell exhibited a temporary improvement in efficiency postrecovery, driven by transient changes in hydrogen, oxygen, and water content.

These findings provide practical insights for addressing transient thermal management, reactant distribution, and water management in PEMFCs for aviation. The parallel branched channel layout with counterflow, suitable for moderate-load conditions, was found to offer a balance between efficiency and simplicity. However, its performance under dynamic aerospace-specific scenarios requires further investigation. Future research should focus on:

- Experimental validation of numerical findings and optimization of PEMFC designs for aerospace applications.
- Exploring alternative flow channel configurations, such as serpentine and hybrid designs, to enhance performance under transient thermal and water management challenges.
- Integrated advanced cooling and humidification systems to improve reliability in extreme aerospace conditions.
- Scaling these findings to larger fuel cell stacks for high-power aviation applications.

This study highlights the potential of PEMFCs as efficient and sustainable energy systems for aviation. Collaborative efforts between researchers, industry, and policymakers will be essential to overcome technical challenges and realize their full potential in aerospace applications.

■ ASSOCIATED CONTENT

Data Availability Statement

No data is associated with this paper.

Supporting Information

The Supporting Information is available free of charge at https://pubs.acs.org/doi/10.1021/acs.energyfuels.4c04834.

Details of simulation setup (methodology). Figures S1−S3 present schematic diagrams supporting the fuel cell, while Figures S4−S16 provide Supporting Information (PDF)

■ AUTHOR INFORMATION

Corresponding Author

Mohammad Alnajideen − *College of Physical Sciences and Engineering, Cardiff University, Cardiff CF24 3AA, U.K.;*

https://doi.org/10.1021/acs.energyfuels.4c04834
Energy Fuels 2025, 39, 7876−7889

orcid.org/0000-0001-9408-6893;
Email: AlnajideenMI@cardiff.ac.uk

Authors

Mehdi Seddiq − *College of Physical Sciences and Engineering, Cardiff University, Cardiff CF24 3AA, U.K.; City University of London, School of Science and Technology, London EC1 V 4PB, U.K.*

Rukshan Navaratne − *College of Physical Sciences and Engineering, Cardiff University, Cardiff CF24 3AA, U.K.*

Complete contact information is available at:
https://pubs.acs.org/10.1021/acs.energyfuels.4c04834

Author Contributions

Mehdi Seddiq: writing—review and editing, writing—original draft, software, methodology, investigation, formal analysis, data curation, conceptualization. **Mohammad Alnajideen**: writing—review and editing, methodology, investigation, formal analysis, visualization, validation, conceptualization. **Rukshan Navaratne**: supervision, resources, project administration, funding acquisition.

Notes

The authors declare no competing financial interest.

■ ACKNOWLEDGMENTS

Cardiff University authors gratefully acknowledge the financial support provided by the Welsh European Funding Office—the Welsh Government in the UK, through the SMART Expertise grant No 82487 for the project titled "Design and development of hybrid electric propulsion system for regional aircraft (DragonFLY)".

■ NOMENCLATURE

A. ampere (A); BP. bipolar plate; CL. catalyst layer; GDL. gas diffusion layer; MEA. membrane electrolyte assembly; PEM. polymer electrolyte membrane; PEMFC. polymer electrolyte membrane fuel cell; V. voltage (Volt)

■ REFERENCES

(1) Baroutaji, A.; Wilberforce, T.; Ramadan, M.; Olabi, A. G. Comprehensive investigation on hydrogen and fuel cell technology in the aviation and aerospace sectors. *Renewable Sustainable Energy Rev.* **2019**, *106*, 31−40.

(2) Guida, D.; Minutillo, M. Design methodology for a PEM fuel cell power system in a more electrical aircraft. *Appl. Energy* **2017**, *192*, 446−456.

(3) Chiara Massaro, M.; Pramotton, S.; Marocco, P.; Monteverde, A. H. A.; Santarelli, M. Optimal design of a hydrogen-powered fuel cell system for aircraft applications. *Energy Convers. Manage.* **2024**, *306*, 118266.

(4) Alaswad, A.; Baroutaji, A.; Achour, H.; Carton, J.; Al Makky, A.; Olabi, A.-G. Developments in fuel cell technologies in the transport sector. *Int. J. Hydrogen Energy* **2016**, *41* (37), 16499−16508.

(5) Arat, H. T.; Sürer, M. G.; Gökpinar, S.; Aydin, K. Conceptual design analysis for a lightweight aircraft with a fuel cell hybrid propulsion system. *Energy Sources, Part A* **2023**, *45* (1), 46−60.

(6) Stambouli, A. B. Fuel cells: The expectations for an environmental-friendly and sustainable source of energy. *Renewable Sustainable Energy Rev.* **2011**, *15* (9), 4507−4520.

(7) Gong, A.; Verstraete, D. Fuel cell propulsion in small fixed-wing unmanned aerial vehicles: Current status and research needs. *Int. J. Hydrogen Energy* **2017**, *42* (33), 21311−21333.

(8) Derbeli, M.; Barambones, O.; Farhat, M.; Ramos-Hernanz, J. A.; Sbita, L. Robust high order sliding mode control for performance improvement of PEM fuel cell power systems. *Int. J. Hydrogen Energy* **2020**, *45* (53), 29222−29234.

(9) Vasilyev, A.; Andrews, J.; Dunnett, S. J.; Jackson, L. M. Dynamic reliability assessment of PEM fuel cell systems. *Reliab. Eng. Syst. Saf.* **2021**, *210*, 107539.

(10) Datta, A. *PEM Fuel Cell MODEL for Conceptual Design of Hydrogen eVTOL Aircraft*; University of Maryland, 2021.

(11) Smith, P. J.; Zhong, Z.; Cain, K. P.; Cashman, J. L.; Debelak, B. W.; Gilligan, R. P.; Hervol, D. S.; O'Meara, C. A.; Green, R. D.; Stalcup, E. J. *Aerospace Regenerative Fuel Cell Fluidic Component Design Challenges*, 2022.

(12) Wang, Y.; Chen, K. S.; Mishler, J.; Cho, S. C.; Adroher, X. C. A review of polymer electrolyte membrane fuel cells: Technology, applications, and needs on fundamental research. *Appl. Energy* **2011**, *88* (4), 981−1007.

(13) Vante, N. A.; Tributsch, H. Energy conversion catalysis using semiconducting transition metal cluster compounds. *Nature* **1986**, *323* (6087), 431−432.

(14) Fernández, J. L.; Raghuveer, V.; Manthiram, A.; Bard, A. J. Pd−Ti and Pd− Co− Au electrocatalysts as a replacement for platinum for oxygen reduction in proton exchange membrane fuel cells. *J. Am. Chem. Soc.* **2005**, *127* (38), 13100−13101.

(15) Bashyam, R.; Zelenay, P. A class of non-precious metal composite catalysts for fuel cells. *Nature* **2006**, *443* (7107), 63−66.

(16) Alaswad, A.; Omran, A.; Sodre, J. R.; Wilberforce, T.; Pignatelli, G.; Dassisti, M.; Baroutaji, A.; Olabi, A. G. Technical and commercial challenges of proton-exchange membrane (PEM) fuel cells. *Energies* **2021**, *14* (1), 144.

(17) Tellez-Cruz, M. M.; Escorihuela, J.; Solorza-Feria, O.; Compañ, V. Proton exchange membrane fuel cells (PEMFCs): Advances and challenges. *Polymers* **2021**, *13* (18), 3064.

(18) Xie, M.; Chu, T.; Wang, T.; Wan, K.; Yang, D.; Li, B.; Ming, P.; Zhang, C. Preparation, performance and challenges of catalyst layer for proton exchange membrane fuel cell. *Membranes* **2021**, *11* (11), 879.

(19) Ahluwalia, R.; Wang, X.; Kwon, J.; Rousseau, A.; Kalinoski, J.; James, B.; Marcinkoski, J. Performance and cost of automotive fuel cell systems with ultra-low platinum loadings. *J. Power Sources* **2011**, *196* (10), 4619−4630.

(20) Wang, Y.; Ruiz Diaz, D. F.; Chen, K. S.; Wang, Z.; Adroher, X. C. Materials, technological status, and fundamentals of PEM fuel cells − A review. *Mater. Today* **2020**, *32*, 178−203.

(21) Morales López, J. *Fuel cell-powered Adaptation of a Light Helicopter Design and Environmental Impact Analysis*; Universitat Politècnica de València, 2022.

(22) Singh, M.; Singla, M. K.; Safaraliev, M.; Singh, K.; Odinaev, I.; Abdel Menaem, A. Advancements and challenges of fuel cell integration in electric vehicles: A comprehensive analysis. *Int. J. Hydrogen Energy* **2024**, *88*, 1386−1397.

(23) Togun, H.; Aljibori, H. S. S.; Abed, A. M.; Biswas, N.; Alshamkhani, M. T.; Niyas, H.; Mohammed, H. I.; Rashid, F. L.; Paul, D. A review on recent advances on improving fuel economy and performance of a fuel cell hybrid electric vehicle. *Int. J. Hydrogen Energy* **2024**, *89*, 22−47.

(24) Liu, Z.; Chen, H.; Zhang, T. Review on system mitigation strategies for start-stop degradation of automotive proton exchange membrane fuel cell. *Appl. Energy* **2022**, *327*, 120058.

(25) Chen, J.; He, H.; Yue, H. A review of plateau environmental adaptation for proton exchange membrane fuel cells. *Int. J. Hydrogen Energy* **2024**, *50*, 744−764.

(26) Li, Y.; Hu, Z.; Liu, H.; Xu, L.; Li, J.; Xu, L.; Ouyang, M. Comprehensive analysis of cathode air pressure of fuel cell powertrain system of aircraft: Performance, efficiency, and control. *Energy Convers. Manage.* **2023**, *283*, 116903.

(27) Gao, S.; Jiang, Y.; Sun, J.; Zhang, Z. Research status and prospect of graphene materials in aviation. *arXiv* **2022**, 2209.08977.

(28) Chalk, S. G.; Miller, J. F.; Wagner, F. W. Challenges for fuel cells in transport applications. *J. Power Sources* **2000**, *86* (1), 40−51.

(29) Ahmadi, P.; Raeesi, M.; Changizian, S.; Teimouri, A.; Khoshnevisan, A. Lifecycle assessment of diesel, diesel-electric and hydrogen fuel cell transit buses with fuel cell degradation and battery aging using machine learning techniques. *Energy* **2022**, *259*, 125003.
(30) Xi, F.; Shen, Y.; Liu, S.; Wang, B.; Liu, X.; Hou, W.; Fu, P.; Zhao, Y.; Miao, P.; Zhang, G.; et al. A 4750 hours' durability investigation of the PEMFC stack based on fuel cell hybrid vehicles conditions. *Int. J. Green Energy* **2024**, *21* (8), 1874−1885.
(31) Moein Jahromi, M.; Heidary, H. Automotive applications of PEM technology. *PEM Fuel Cells* **2022**, 347−405.
(32) Xing, Y.; Li, H.; Avgouropoulos, G. Research progress of proton exchange membrane failure and mitigation strategies. *Materials* **2021**, *14* (10), 2591.
(33) Soleimani Moghaddam, M.; Bahari, A.; Houshani, M.; Jafari, A.; Tapeh, S. M. T. A review on progress in the field of conditioning of polymer fuel cell stacks. *J. Power Sources* **2024**, *621*, 235300.
(34) Qasem, N. A.; Abdulrahman, G. A. A recent comprehensive review of fuel cells: history, types, and applications. *Int. J. Energy Res.* **2024**, *2024* (1), 7271748.
(35) Hinds, G. *Performance and Durability of PEM Fuel Cells: A Review*, 2004.
(36) Veeranjaneyulu, K.; Joshi, S.; Devalla, V.; Kiran, K. S.; Khushal. Recent advancements of PEMFC in transport applications. *AIP Conf. Proc.* **2023**, *2492* (1), 050019.
(37) Kurnia, J. C.; Sasmito, A. P.; Shamim, T. Advances in proton exchange membrane fuel cell with dead-end anode operation: A review. *Appl. Energy* **2019**, *252*, 113416.
(38) Chalk, S. G.; Miller, J. F. Key challenges and recent progress in batteries, fuel cells, and hydrogen storage for clean energy systems. *J. Power Sources* **2006**, *159* (1), 73−80.
(39) Pei, P.; Wang, M.; Chen, D.; Ren, P.; Zhang, L. Key technologies for polymer electrolyte membrane fuel cell systems fueled impure hydrogen. *Prog. Nat. Sci.:Mater. Int.* **2020**, *30* (6), 751−763.
(40) Wang, G.; Yu, Y.; Liu, H.; Gong, C.; Wen, S.; Wang, X.; Tu, Z. Progress on design and development of polymer electrolyte membrane fuel cell systems for vehicle applications: A review. *Fuel Process. Technol.* **2018**, *179*, 203−228.
(41) Borup, R. L.; Kusoglu, A.; Neyerlin, K. C.; Mukundan, R.; Ahluwalia, R. K.; Cullen, D. A.; More, K. L.; Weber, A. Z.; Myers, D. J. Recent developments in catalyst-related PEM fuel cell durability. *Curr. Opin. Electrochem.* **2020**, *21*, 192−200.
(42) Mo, S.; Du, L.; Huang, Z.; Chen, J.; Zhou, Y.; Wu, P.; Meng, L.; Wang, N.; Xing, L.; Zhao, M.; et al. Recent advances on PEM fuel cells: from key materials to membrane electrode assembly. *Electrochem. Energy Rev.* **2023**, *6* (1), 28.
(43) Xie, Z.; Wang, J.; Zhao, G.; Zhang, Q.; Fan, H.; Zeng, A.; Ding, W. A review on durability of key components of PEM fuel cells. *Catal. Sci. Technol.* **2024**, *14*, 4420−4431.
(44) Zhang, Z.; Mao, J.; Liu, Z. Advancements and insights in thermal and water management of proton exchange membrane fuel cells: Challenges and prospects. *Int. Commun. Heat Mass Transfer* **2024**, *153*, 107376.
(45) Breeze, P. The Proton Exchange Membrane Fuel Cell. In *Fuel Cells*; Breeze, P., Ed.; Academic Press, 2017; pp 33−43. Chapter 4.
(46) Miller, M.; Bazylak, A. A review of polymer electrolyte membrane fuel cell stack testing. *J. Power Sources* **2011**, *196* (2), 601−613.
(47) Wang, X.; Ma, Y.; Gao, J.; Li, T.; Jiang, G.; Sun, Z. Review on water management methods for proton exchange membrane fuel cells. *Int. J. Hydrogen Energy* **2021**, *46* (22), 12206−12229.
(48) Liu, Q.; Lan, F.; Chen, J.; Zeng, C.; Wang, J. A review of proton exchange membrane fuel cell water management: Membrane electrode assembly. *J. Power Sources* **2022**, *517*, 230723.
(49) Zhang, C.; Liu, Z.; Zhou, W.; Chan, S. H.; Wang, Y. Dynamic performance of a high-temperature PEM fuel cell e An experimental study. *Energy* **2015**, *90*, 1949−1955.
(50) Saleh, I.; Ali, R.; Zhang, H. Experimental Testing and Validation of the Mathematical Model for a Self-Humidifying PEM Fuel Cell. *J. Mater. Sci. Chem. Eng.* **2018**, *06*, 202−218.
(51) Zhao, X.; Zhou, Y.; Wang, L.; Pan, B.; Wang, R.; Wang, L. Classification, summarization and perspective on modeling techniques for polymer electrolyte membrane fuel cell. *Int. J. Hydrogen Energy* **2023**, *48* (57), 21864−21885.
(52) Franco, A. Modelling and analysis of degradation phenomena in polymer electrolyte membrane fuel cells. *Polymer Electrolyte Membrane Direct Methanol Fuel Cell Technology* **2012**, 291−367.
(53) Shah, A. A.; Luo, K.; Ralph, T.; Walsh, F. Recent trends and developments in polymer electrolyte membrane fuel cell modelling. *Electrochim. Acta* **2011**, *56* (11), 3731−3757.
(54) Akimoto, Y.; Okajima, K. Semi-Empirical Equation of PEMFC Considering Operation Temperature. *Energy Technol.* **2014**, *1*, 91−96.
(55) Yerramalla, S.; Davari, A.; Feliachi, A.; Biswas, T. Modeling and simulation of the dynamic behavior of a polymer electrolyte membrane fuel cell. *J. Power Sources* **2003**, *124* (1), 104−113.
(56) Pathapati, P. R.; Xue, X.; Tang, J. A new dynamic model for predicting transient phenomena in a PEM fuel cell system. *Renewable Energy* **2005**, *30*, 1−22.
(57) Shamardina, O.; Kondratenko, M. S.; Chertovich, A. V.; Kulikovsky, A. A. A simple transient model for a high temperature PEM fuel cell impedance. *Int. J. Hydrogen Energy* **2014**, *39*, 2224−2235.
(58) Rabbani, A.; Rokni, M. Effect of nitrogen crossover on purging strategy in PEM fuel cell systems. *Appl. Energy* **2013**, *111*, 1061−1070.
(59) Lan, T.; Strunz, K. Modeling of multi-physics transients in PEM fuel cells using equivalent circuits for consistent representation of electric, pneumatic, and thermal quantities. *Int. J. Electr. Power Energy Syst* **2020**, *119*, 105803.
(60) Zou, W.-J.; Kim, Y.-B. Temperature Control for a 5 kW Water-Cooled PEM Fuel Cell System for a Household Application. *IEEE Access* **2019**, *7*, 144826−144835.
(61) Ceylan, C.; Devrim, Y. Design and simulation of the PV/PEM fuel cell based hybrid energy system using MATLAB/Simulink for greenhouse application. *Int. J. Hydrogen Energy* **2021**, *46*, 22092−22106.
(62) Yan, W.-M.; Li, H.-Y.; Weng, W.-C. Transient mass transport and cell performance of a PEM fuel cell. *Int. J. Heat Mass Transfer* **2017**, *107*, 646−656.
(63) Goshtasbi, A.; García-Salaberri, P.; Chen, J.; Talukdar, K.; Sanchez, D. G.; Ersal, T. Through-the-Membrane Transient Phenomena in PEM Fuel Cells: A Modeling Study. *J. Electrochem. Soc.* **2019**, *166* (7), F3154−F3179.
(64) Bodner, M.; Penga, Ž.; Ladreiter, W.; HeidingerHacker, M. V.; Viktor, H. Simulation-Assisted Determination of the Start-Up Time of a Polymer Electrolyte Fuel Cell. *Energies* **2021**, *14*, 7929.
(65) Wang, Q.; Tang, F.; Li, B.; Dai, H.; Zheng, J. P.; Zhang, C.; Ming, P. Study on the thermal transient of cathode catalyst layer in proton exchange membrane fuel cell under dynamic loading with a two-dimensional model. *Chem. Eng. J.* **2022**, *433*, 133667.
(66) Kravos, A.; Ambroz, K.; Penga, Z.; Frano, B.; Katrasnik, T. Real-time capable transient model of liquid water dynamics in proton exchange membrane Fuel Cells. *J. Power Sources* **2022**, *541*, 231598.
(67) Barbir, F. *PEM Fuel Cells, Theory and Practice*; Elsevier Inc., 2013.
(68) Babic, U.; Suermann, M.; Büchi, F. N.; Gubler, L.; Schmidt, T. J. Critical review—identifying critical gaps for polymer electrolyte water electrolysis development. *J. Electrochem. Soc.* **2017**, *164* (4), F387.
(69) Djilali, N.; Lu, D. Influence of heat transfer on gas and water transport in fuel cells. *Int. J. Therm. Sci.* **2002**, *41* (1), 29−40.
(70) Ji, M.; Wei, Z. A review of water management in polymer electrolyte membrane fuel cells. *Energies* **2009**, *2* (4), 1057−1106.
(71) Yan, Q.; Toghiani, H.; Lee, Y.-W.; Liang, K.; Causey, H. Effect of sub-freezing temperatures on a PEM fuel cell performance, startup and fuel cell components. *J. Power Sources* **2006**, *160*, 1242−1250.

https://doi.org/10.1021/acs.energyfuels.4c04834
Energy Fuels 2025, 39, 7876−7889

(72) Adzakpa, K. P.; Ramousse, J.; Dubé, Y.; Akremi, H.; Agbossou, K.; Dostie, M.; Poulin, A.; Fournier, M. Transient air cooling thermal modeling of a PEM fuel cell. *J. Power Sources* **2008**, *179*, 164−176.
(73) Ondrejička, K.; Ferencey, V.; Stromko, M. Modeling of the air-cooled PEM fuel cell. *IFAC PapersOnLine* **2019**, *52* (27), 98−105.
(74) Manso, A.; Marzo, F.; Barranco, J.; Garikano, X.; Garmendia Mujika, M. Influence of geometric parameters of the flow fields on the performance of a PEM fuel cell. A review. *Int. J. Hydrogen Energy* **2012**, *37* (20), 15256−15287.
(75) Cooper, N. J. *Experimental Testing and Characterization of High Power Flow Field PEM Fuel Cell Design Parameters*; University of California: Davis, 2016.
(76) Jeon, D. H.; Greenway, S.; Shimpalee, S.; Van Zee, J. W. The effect of serpentine flow-field designs on PEM fuel cell performance. *Int. J. Hydrogen Energy* **2008**, *33* (3), 1052−1066.
(77) Dhahad, H. A.; Alawee, W. H.; Hassan, A. K. Experimental study of the effect of flow field design to PEM fuel cells performance. *Renew. Energy Focus* **2019**, *30*, 71−77.
(78) Wang, Y.; Wang, S.; Liu, S.; Li, H.; Zhu, K. Optimization of reactants relative humidity for high performance of polymer electrolyte membrane fuel cells with co-flow and counter-flow configurations. *Energy Convers. Manage.* **2020**, *205*, 112369.
(79) Rocha, C.; Knöri, T.; Ribeirinha, P.; Gazdzicki, P. A review on flow field design for proton exchange membrane fuel cells: Challenges to increase the active area for MW applications. *Renewable Sustainable Energy Rev.* **2024**, *192*, 114198.
(80) Chen, Q.; Zhang, G.; Zhang, X.; Sun, C.; Jiao, K.; Wang, Y. Thermal management of polymer electrolyte membrane fuel cells: A review of cooling methods, material properties, and durability. *Appl. Energy* **2021**, *286*, 116496.
(81) Ahmed, M.; Shusheng, X. Comprehensive review of serpentine flow fields for effective thermal management of proton exchange membrane fuel cell. *Heliyon* **2024**, *10* (21), No. e39793.
(82) Liao, Z.; Wei, L.; Dafalla, A. M.; Guo, J.; Jiang, F. Analysis of the impact of flow field arrangement on the performance of PEMFC with zigzag-shaped channels. *Int. J. Heat Mass Transfer* **2021**, *181*, 121900.
(83) Wang, Y.; Leung, D. Y.; Zhang, H.; Xuan, J.; Wang, H. Numerical and experimental comparative study of microfluidic fuel cells with different flow configurations: Co-flow vs. counter-flow cell. *Appl. Energy* **2017**, *203*, 535−548.
(84) Lu, G.; Liu, M.; Su, X.; Zheng, T.; Luan, Y.; Fan, W.; Cui, H.; Liu, Z. Study on counter-flow mass transfer characteristics and performance optimization of commercial large-scale proton exchange membrane fuel cells. *Appl. Energy* **2024**, *359*, 122743.
(85) Shao, Q.; Wang, M.; Xu, N. Influences of Co-Flow and Counter-Flow Modes of Reactant Flow Arrangement on a PEMFC at Start-Up. *Comput. Model. Eng. Sci.* **2024**, *139* (2), 1337−1356.
(86) Pan, W.; Wang, P.; Chen, X.; Wang, F.; Dai, G. Combined effects of flow channel configuration and operating conditions on PEM fuel cell performance. *Energy Convers. Manage.* **2020**, *220*, 113046.
(87) Wang, J.; Wang, H. Discrete approach for flow field designs of parallel channel configurations in fuel cells. *Int. J. Hydrogen Energy* **2012**, *37* (14), 10881−10897.
(88) Wang, Y.; Liao, X.; Liu, G.; Xu, H.; Guan, C.; Wang, H.; Li, H.; He, W.; Qin, Y. Review of flow field designs for polymer electrolyte membrane fuel cells. *Energies* **2023**, *16* (10), 4207.
(89) Choi, J.; Park, Y.; Park, J.; Kim, C.; Heo, S.; Kim, S.-D.; Ju, H. Innovative flow field design strategies for performance optimization in polymer electrolyte membrane fuel cells. *Appl. Energy* **2025**, *377*, 124551.
(90) Pedapati, P. R.; Dhanushkodi, S. R.; Chidambaram, R. K.; Taler, D.; Sobota, T.; Taler, J. Design and Manufacturing Challenges in PEMFC Flow Fields—A Review. *Energies* **2024**, *17* (14), 3499.
(91) Edwards, H.; Pereira, M. P.; Gharaie, S.; Omrani, R.; Shabani, B. Computational fluid dynamics modelling of proton exchange membrane fuel cells: Accuracy and time efficiency. *Int. J. Hydrogen Energy* **2024**, *50*, 682−710.
(92) Dyantyi, N.; Parsons, A.; Sita, C.; Pasupathi, S. PEMFC for aeronautic applications: A review on the durability aspects. *Open Eng.* **2017**, *7* (1), 287−302.
(93) Spiegel, C. *PEM Fuel Cell Modeling and Simulation Using MATLAB*; Elsevier, 2011.
(94) Kulikovsky, A. A. *Analytical Modelling of Fuel Cells*; Elsevier, 2019.
(95) *ANSYS Fluent Theory Guide*. ANSYS, Inc: Canonsburg, PA, 2021.
(96) Najmi, A.-U.-H.; Anyanwu, I. S.; Xie, X.; Liu, Z.; Jiao, K. Experimental investigation and optimization of proton exchange membrane fuel cell using different flow fields. *Energy* **2021**, *217*, 119313.

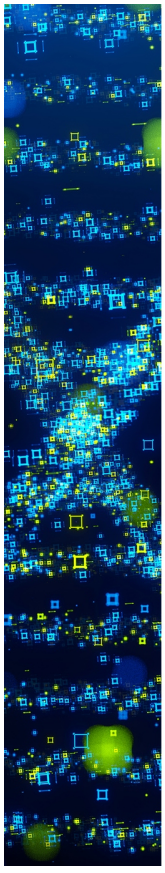
CAS BIOFINDER DISCOVERY PLATFORM™
STOP DIGGING THROUGH DATA —START MAKING DISCOVERIES
CAS BioFinder helps you find the right biological insights in seconds
Start your search
CAS
A division of the American Chemical Society

https://doi.org/10.1021/acs.energyfuels.4c04834
Energy Fuels 2025, 39, 7876−7889